

Engineering a multi-level bath for transmon with three-wave mixing and parametric drives

Xi Cao,^{1,*} Maria Mucci,^{1,†} Gangqiang Liu,¹ David Pekker,¹ and Michael Hatridge^{1,‡}

¹*Department of Physics and Astronomy, University of Pittsburgh, Pittsburgh, PA, 15260, USA*

(Dated: August 1, 2024)

A photonic system with a tunable bath environment provides an extra degree of freedom for quantum simulators. Such a system can be realized by parametrically modulating the coupling between the system and bath. In this letter, by coupling a transmon qubit to a lossy Superconducting Non-linear Asymmetric Inductive eLement (SNAIL) mode, we experimentally create a tunable chemical potential for the qubit mode. We show that the qubit can be thermalized to equilibrium with different population distributions under different parametric pumping conditions. We further extend our method to the third level of the transmon, showing its practical use beyond the simple two-level case. Our results provide a useful tool that can be readily integrated with quantum simulators that would benefit from a non-trivial photon population distribution.

A quantum simulator [1] can address complex problems in various domains of physics, including quantum materials simulation [2, 3], quantum chemistry [4], quantum transport [5, 6], many-body dynamics [7, 8], and even black holes [9], by mapping a problem that is otherwise difficult to probe or track in its original setting to an engineered quantum system over which experimenters have good control. Photonic excitation provides an important degree of freedom in many quantum simulating platforms, such as microwave superconducting circuits [10], trapped ions [11], and optical photon-based quantum machines [12]. Therefore, the ability to engineer different properties of a photonic system becomes essential in these quantum simulators. A tunable chemical potential, or more generally, a controllable photonic bath, is of great interest. A photonic system with a well defined chemical potential has a fixed occupation number and can thus be used to simulate entities with a conserved particle number, such as electrons and atoms [13–15]. However, a well-defined occupation number, and thus the concept of a chemical potential, does not arise naturally in a photonic system. In Planck’s initial study on the thermodynamics of blackbody radiation [16], a chemical potential term is absent due to the photons’ absorption and emission by the walls of their container. Later it came to be understood that in systems without such walls, photons can acquire a non-zero chemical potential. For example in semiconductor junctions, the chemical potential of photons arises due to interactions between electrons and holes [17]. More recently, there have been demonstrations of non-zero chemical potential in a dye-filled optical cavity that forms a Bose-Einstein condensate [18, 19].

Superconducting circuits and circuit quantum electrodynamics (cQED) [10] provide a promising platform for

the investigation of this topic in the microwave domain. The strong coupling between superconducting circuits and their environment, and controllable parametric interactions between different circuit modes, enable the manipulation of mode populations with bath engineering techniques. Demonstrations include: fast qubit reset by forcing it to its ground state with appropriate drives [20], stabilizing a qubit to an arbitrary state [21], and in particular, stabilizing a photonic system with a non-trivial photonic state [22]. Based on these remarkable results, it is natural to consider the implementation of a tunable chemical potential in a photonic system, or a tunable photonic bath.

In this letter, we experimentally demonstrate a multi-level bath for a transmon qubit. We start by coupling it to a lossy mode via a mode conversion process and a two-mode squeezing process within its $|g\rangle$ - $|e\rangle$ manifold. The transmon is treated as a two-level system whose dissipation is engineered by tuning the strengths of these two parametric processes. This tunable dissipation sets the average photon number in the qubit mode, and by constraining this photonic mode in a two-level setting, we are effectively realizing a population statistic in the form of Fermi-Dirac distribution with a chemical potential. We verify this behavior by stabilizing the qubit to various equilibrium states with different population distributions, including a population inverted state which cannot be achieved by coupling to a natural bath at positive temperatures.

Furthermore, the anharmonic multi-level nature of the transmon allows us to go beyond the simple two-level model. We extend our parametric bath engineering technique to the third energy level of the transmon, creating a non-trivial photonic state in a three-level system. This allows us to enter the regime of Gentile statistics [23–25], a generalization of Fermi-Dirac and Bose-Einstein statistics where the mode maximum occupation number (here photons in a qubit) can be set between one (Fermions) and infinity (Bosons). Our work demonstrates a promising method to create an effective *in situ* tunable chemical potential for a photonic qubit system, as well as generate

* These authors contributed equally; Now at: Department of Physics, University of Illinois Urbana-Champaign, Champaign, IL, USA

† These authors contributed equally

‡ email: hatridge@pitt.edu

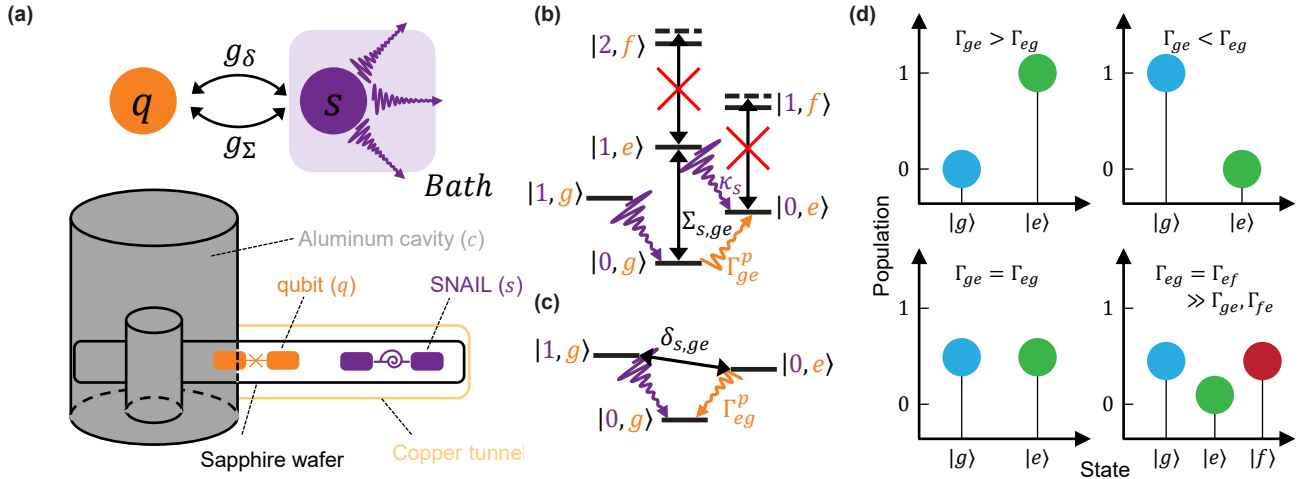


Figure 1. Experiment concept and schematic. (a) Interactions between the electromagnetic modes in the system: the readout cavity mode c , transmon qubit mode q and SNAIL-mon mode s . All three modes have a dedicated rf-coupling port (not pictured). (b), (c) Level diagram of the system. Purple numbers represent the state of the SNAIL-mon and orange letters the state of the qubit. (b) Heating process with the Σ drive. The system starts in its joint ground state and is brought to $|1, e\rangle$ with the Σ pump. This entire process is observed as an effective parametric heating rate of Γ_{ge}^p . (c) Cooling process with the δ drive. The qubit is prepared to $|e\rangle$ and the $\delta_{s,ge}$ drive converts the excitation to the SNAIL-mon, which quickly decays. This process creates an effective parametric cooling rate Γ_{eg}^p to empty the qubit. (d) Tuning the chemical potential with parametric processes. Enhancing Γ_{ge} to invert the transmon, achieving negative temperatures (top left). Enhancing Γ_{eg} to cool the transmon to low, positive temperatures (top right). Infinite temperature by balancing Γ_{ge} and Γ_{eg} (bottom left). ‘Non-thermal’ states in which the transmon relaxes away from $|e\rangle$ but has no preference between $|g\rangle$ and $|f\rangle$ (bottom right).

arbitrary multi-level state configurations in the scope of certain intermediate statistics beyond Bose–Einstein and Fermi–Dirac statistics.

Theory: We begin by constructing a model that reflects our objective: we aim to create a tunable multi-level bath for a photonic system. Inspired by a proposal from Hafezi *et al.* [26], this can be realized by parametrically coupling a microwave mode to another lossy mode. We consider a system that consists of a transmon qubit q [27] capacitively coupled to a SNAIL-mon mode s [28] (a SNAIL element shunted by a large capacitor) as shown in the top panel of Fig. 1(a). We aim to create a tunable bath for the qubit mode, and the SNAIL-mon is used both as a three-wave mixing element and the lossy mode. The qubit is also coupled to a 3D cavity for dispersive readout [29]. We note that while our experiment is implemented with cQED, the general model of the design is fundamentally platform-independent.

Central to our protocol are the parametric interactions between the qubit and the SNAIL-mon. In particular, we are interested in two types of interactions: two-mode squeezing and mode conversion, whose Hamiltonian are given by [30–32]:

$$H_{\text{tms}} = g_\Sigma(s^\dagger q^\dagger + \text{h.c.}), \quad (1)$$

$$H_{\text{bs}} = g_\delta(s^\dagger q + \text{h.c.}), \quad (2)$$

where s and q are the annihilation operators of the SNAIL-mon and qubit mode respectively, g_Σ and g_δ are the interaction strength of the corresponding processes, which can be controlled via external drives. The sub-

scripts are labelled Σ and δ due to a pump at summation/difference frequency of the SNAIL-mon (ω_s) and qubit (ω_q), i.e., $\omega_p = \omega_s \pm \omega_q$, is needed for each process respectively. A detailed derivation of above equations can be found in Appendix B.

Equations 1 and 2 give a general description of the two processes between the linear modes. In our case, however, the anharmonicity of the transmon qubit needs to be considered. Let us take the two-mode squeezing case as an example. As shown in Fig. 1(b), the two-mode squeezing pump creates a coherent process between the $|0, g\rangle$ and $|1, e\rangle$ (the joint ket notation follows the convention of $|\text{SNAIL-mon}(number), \text{qubit}(letter)\rangle$ throughout the paper). When both modes are linear, the pump will also drive the similar processes, such as $|1, e\rangle \leftrightarrow |2, f\rangle$, $|2, f\rangle \leftrightarrow |3, h\rangle$ and etc. However, the transmon’s large anharmonicity makes the pump off-resonance for these processes and thus forbids (at least to the leading order) them to appear in the rotating frame. It is then necessary to re-write Eqs. 1 and 2 for individual qubit levels. For two adjacent qubit levels $|i\rangle$ and $|i+1\rangle$, the respective interaction Hamiltonian terms are given by:

$$H_{\Sigma_{s,i,i+1}} = g_{\Sigma_{s,i,i+1}} s^\dagger |i+1\rangle \langle i| + \text{h.c.}, \quad (3)$$

$$H_{\delta_{s,i,i+1}} = g_{\delta_{s,i,i+1}} s^\dagger |i\rangle \langle i+1| + \text{h.c.}, \quad (4)$$

where $g_{\Sigma_{s,i,i+1}}$ and $g_{\delta_{s,i,i+1}}$ are the effective coupling rates of the two individual processes (Appendix D), with the corresponding pump frequencies: $\omega_{\Sigma_{s,i,i+1}} = \omega_s + \omega_{i,i+1}$ and $\omega_{\delta_{s,i,i+1}} = \omega_s - \omega_{i,i+1}$. We have chosen to replace the

usual transmon raising/lowering operators in these equations with ket-bra notation to make clear that each parametric drive frequency links only a single pair of transmon levels. Because of the frequency selective nature of the parametric processes, multiple parametric interactions can be activated at the same time by simultaneously applying multiple pumps.

To understand how to engineer the transmon bath, let us first consider a simple case where the transmon is treated as a two-level system. We implement an effective tunable chemical potential for the transmon mode within this two-level manifold. The crucial step is to constrain the mode occupation number, which is implemented by combining the parametric processes and SNAIL-mon dissipation. As shown in Fig. 1(b), a pump at $\omega_p = \omega_{\Sigma_{s,ge}}$ coherently brings the system from $|0, g\rangle$ to $|1, e\rangle$. When the SNAIL-mon decay rate is much larger than the other relevant rates, i.e., $\kappa_s \gg g_{\Sigma_{s,ge}}, 1/T_1^q$, the system quickly falls into $|0, e\rangle$, effectively constraining the transmon occupation number at 1. Similarly, as shown in Fig. 1(c), a pump at $\omega_p = \omega_{\delta_{s,ge}}$ will effectively constrain the transmon occupation number at 0. We refer to these two processes as parametric “heating” and “cooling”, as they push the transmon to a higher and lower energy state respectively.

The tunable chemical potential can be realized by applying both pumps simultaneously. By controlling the effective rates of the two processes, we can thermalize the transmon to an arbitrary equilibrium state, as shown in Fig. 1(d). We show that (Appendix C), the density matrix of the equilibrium state can be described by a grand canonical ensemble:

$$\rho = Z(\beta, \mu)^{-1} e^{-\beta(\frac{\omega_s}{2}\sigma_q^z - \frac{\mu}{2}\sigma_q^z)}, \quad (5)$$

where $Z(\beta, \mu) = \text{Tr}[e^{-\beta(\frac{\omega_s}{2}\sigma_q^z - \frac{\mu}{2}\sigma_q^z)}]$, σ_q^z is the Pauli z operator for the qubit, and $\beta = 1/kT$ where k is the Boltzmann constant, and T is the SNAIL-mon temperature. The chemical potential μ is given by:

$$\mu = \frac{1}{\beta} \ln \left(\frac{g_{\Sigma_{s,ge}}^2 e^{\beta \hbar \omega_s} + g_{\delta_{s,ge}}^2}{g_{\Sigma_{s,ge}}^2 e^{-\beta \hbar \omega_s} + g_{\delta_{s,ge}}^2} \right), \quad (6)$$

which is a function of the parametric interaction strengths – both quantities that can be externally controlled. However, we would like to point out two important caveats.

First, when deriving Eq. 5 and 6, we assume that the qubit only exchanges energy with environment via the SNAIL-mon mode. In practice, the qubit can also thermalize through other channels at different temperatures, whose rates will add to the parametrically induced ones. We minimize this effect by using a qubit that is much more coherent than the SNAIL-mon. Second, each decay event is heralded by a photon in the SNAIL-mon mode, and so we must take into account the effects of distinguishability of these photons when several processes create these SNAIL-mon excitations at the same time. For example, some engineered bosonic decay processes [33]

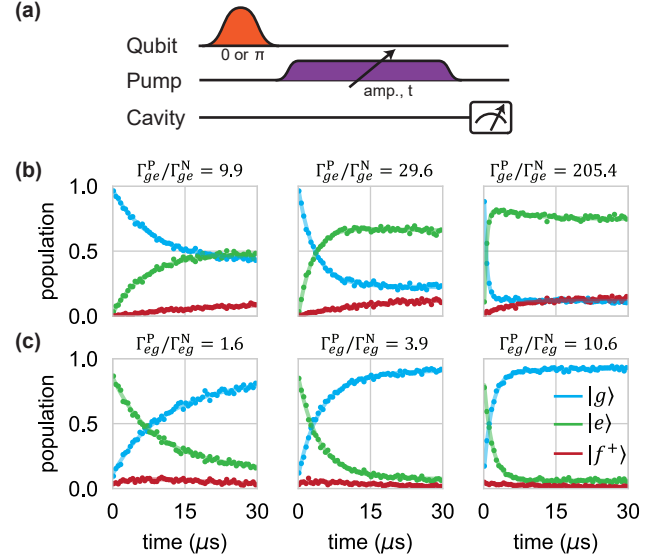


Figure 2. Result of heating and cooling processes. (a) Pulse sequence of the experiment: First, the qubit is initialized in the ground (“heating”) or excited (“cooling”) state. Then the corresponding parametric pump is turned on while sweeping its amplitude and duration. The qubit is measured after the pump is off. (b) Qubit state populations (blue $|g\rangle$, green $|e\rangle$ and red $|f^+\rangle$) as a function of time in the heating process with increasing pump strength $g_{\Sigma_{s,ge}}$, left to right. (c) Qubit state populations as a function of time in the cooling process with increasing pump strength $g_{\delta_{s,ge}}$. All experiment data is fit to a semi-classical model (solid line, see Appendix D) to extract the coupling strengths and rates.

require photon indistinguishability, as the decay operator should protect a manifold of states. In this work, however, we focus on distinguishable photons in our finite temperature bath so that each heating/cooling event is uncorrelated with others. One method to ensure distinguishability is to use unique lossy modes for each process, but this requires greater hardware. Instead, we simply must take care to tune our drives to use the SNAIL-mon’s broad bandwidth to create deliberately different SNAIL-mon excitations for each parametric process.

Experiment: Our experiment scheme is shown in the lower panel of Fig. 1(a). The lossy SNAIL-mon has a bandwidth of 12.98 MHz, and transmon’s natural decay and heating rates are: $\Gamma_{ge}^N/2\pi = 1.22$ kHz, $\Gamma_{eg}^N/2\pi = 8.28$ kHz, $\Gamma_{ef}^N/2\pi = 2.20$ kHz, and $\Gamma_{fe}^N/2\pi = 12.27$ kHz. Other relevant circuit parameters are given in Appendix A. A Traveling Wave Parametric Amplifier (TWPA) [34] is used for single shot readout and transmon state differentiation. We perform a three-part division on the readout data, and label all states from $|f\rangle$ and beyond as $|f^+\rangle$.

We first demonstrate the effect of the “heating” and “cooling” drives. In the heating experiments, the qubit is initialized in its $|g\rangle$ state. We apply the $\Sigma_{s,ge}$ drive while sweeping its strength and duration before the qubit

measurement, as shown in Fig. 2(a). The measurement results of the heating process for different pump strengths are shown in Fig. 2(b), where the qubit state population is plotted as a function of pump duration. The pump strength increases from left to right, resulting in a rise of the heating rate ($\Gamma_{ge}^p/\Gamma_{ge}^N = 9.9, 29.6, 205.4$ respectively) as expected. The rate is extracted from a semi-classical model (solid line, see Appendix D). The qubit also populates the $|f^+\rangle$ state to some extent, which we attribute to the qubit's finite (undriven) temperature that excites the qubit from the $|e\rangle$ to $|f\rangle$ state. In addition, a strong enough pump could also lead to extra parametric heating due to its finite spectral weight on the transmon's higher transition.

We emphasise that, for strong heating drives, the qubit population inverts, rather than spreading to states $|f\rangle$ and higher, the scenario typically achieved by physically heating it. This indicates that our scheme indeed creates a finite chemical potential rather than simply changes the effective temperature of the qubit. More, the system, from the point-of-view of joint SAIL-qubit states, forms a traditional lambda structure with a trapped excited state, making it suitable for single-“atom” masing experiments [35]. Unlike previous implementations, which for instance use a lossy cavity mode and Purcell decay to invert a qubit [22], we require no special mixing frequencies, are compatible with a wide range of qubit frequencies, and can readily access higher excitation states of the transmon.

In cooling experiments, the qubit is initialized in the $|e\rangle$ state. Then the $\delta_{s,ge}$ pump is applied to the system with various pump strengths and pump durations, as shown in Fig. 2(a). The measurement results of the cooling process are shown in Fig. 2(d-f). For each panel from left to right, the transmon thermalizes to its equilibrium state faster as the pump strength increases ($\Gamma_{eg}^p/\Gamma_{eg}^N = 1.6, 3.9, 10.6$ respectively). In contrast to [20] where both the qubit and cavity are driven to force the qubit fully into the $|g\rangle$ state, our method allows us to determine the $|g\rangle$ probability and only requires one drive on the SAIL-mon. Unlike the heating experiment, there is not a rise in the $|f^+\rangle$ state because we are actively pushing the qubit to the ground state and there is no parametric processes that can bring the transmon to the $|f^+\rangle$ state at a frequency near the $\delta_{s,ge}$ pump.

We have demonstrated our control over each single parametric process with the heating and cooling results by establishing the equilibrium states with different chemical potentials. We note that the difference in the final distribution for different single pump strengths does not conflict with Eq. 5 for the case with $g_\Sigma = 0$ or $g_\delta = 0$, as the qubit also directly couples to the environment weakly in practice. To extend the utility of our setup as a tunable photonic bath in a larger system, a demonstration of the full control over the transmon's thermalization process is necessary. That is, we need to be able to set both the final equilibrium state distribution as well as the thermalization rate.

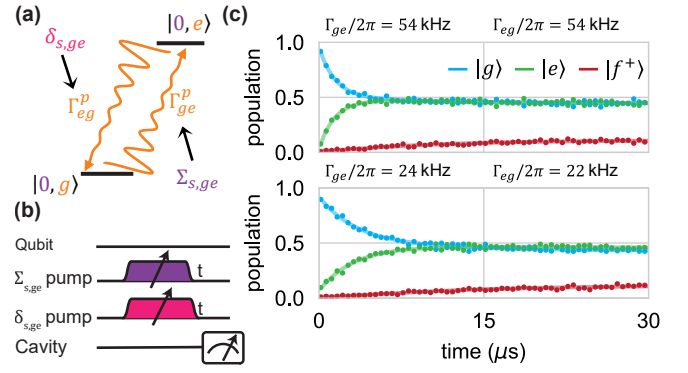


Figure 3. Heating and cooling balance. (a) Schematic of the process. Both Σ and δ pumps are applied to the system simultaneously to reach a mixed 50% $|g\rangle$ - 50% $|e\rangle$ state by balancing the total up- and down-going rates. (b) Pulse sequence of the experiment: First, qubit is initialized in the ground (“heating”) or excited (“cooling”) state. Then both the $\Sigma_{s,ge}$ and $\delta_{s,ge}$ pumps are turned on for different duration. The qubit is measured after the pump is off. (c) Qubit state populations and rate fitting as a function of time for two different pump settings. The qubit is prepared in $|g\rangle$ and thermalized to a nearly-equal thermal mixture of $|g\rangle$ and $|e\rangle$ states. Multiple parametric processes independently control both the relaxation rates and the final thermal state populations.

Therefore we next consider the case where both pumps are applied. As shown in Fig. 3(a), when both the $\Sigma_{s,ge}$ and $\delta_{s,ge}$ drives are on, the two processes happen at the same time with different rates set by their respective pump strengths. The system is initialized in the state $|g, 0\rangle$, then both pumps are applied for a certain duration, followed by a dispersive transmon measurement, as shown in Fig. 3(b). In Fig. 3(c), we show the transmon population as a function of pump length for two sets of heating and cooling rates (top: $\Gamma_{ge}^p/2\pi = 54$ kHz, $\Gamma_{eg}^p/2\pi = 54$ kHz, and bottom: $\Gamma_{ge}^p/2\pi = 24$ kHz, $\Gamma_{eg}^p/2\pi = 22$ kHz). The pump conditions are chosen such that the ratio between the two rates are close to 1 ($\Gamma_{ge}^p/\Gamma_{eg}^p \sim 1$). As expected from Eq. 5 and 6, the transmon thermalizes to the same mixed 50% $|g\rangle$ - 50% $|e\rangle$ state (up to the residual population in the $|f^+\rangle$ state). However, the thermalization rates are different due to the difference in the parametric drive strengths. In addition, the data in the supplementary Fig. 8 shows that by tuning the ratio between the two rates, we are able to set the transmon equilibrium with arbitrary population distribution. This confirms our full control over the transmon bath, in the equilibrium state as well as the thermalization rates, which extends its potential utility as an exotic bath in larger quantum simulators.

We note that because the SAIL-mon is very lossy, and thus has a large bandwidth, it is easy to create distinguishable photons. This is the general case unless great care is taken to match the two pump frequencies to create identical excitation frequencies in the SAIL-mon. In this latter case, certain states of the qubit become

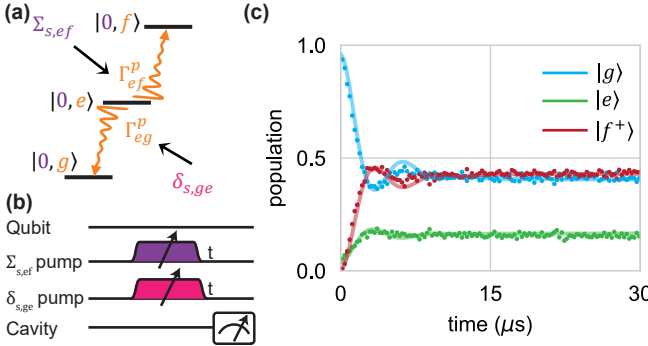


Figure 4. Bath engineering for a three-level qubit. (a) Schematic of the process. Both $\delta_{s,ge}$ and $\Sigma_{s,ef}$ pumps are simultaneously applied with matched rates away from $|e\rangle$ to achieve a mixed state with 50% $|g\rangle$ - 50% $|f^+\rangle$. This cannot be achieved by thermalizing a three-level system to a natural heat bath. (b) Pulse sequence of the experiment: First, the qubit is initialized in the excited state. Then both the $\Sigma_{s,ef}$ and $\delta_{s,ge}$ pumps are turned on for different duration. The qubit is measured after the pump is off. (c) Qubit state populations as a function of time under both pumps with the qubit initially prepared in $|g\rangle$. The $|e\rangle$ population is nontrivial due to contributions of qubit decay from $|f^+\rangle$ and thermal excitations from $|g\rangle$.

'dark' to the parametric process, and the overall behavior changes dramatically. We have separately investigated this in a similar sample [36]. However, experimental observation of these effects is greatly hindered by our ability to maintain a stable set of microwave phases among the qubit and parametric tones; attempts to measure these dark states with conventional few-hundred MHz bandwidth AWGs yielded inconclusive results due to rapid phase drifts; after the conclusion of this experiment we have recently realized fully stable drives which allow us to observe these dark states using high-speed RFSoC electronics and the QICK platform [37].

Finally, we extend our protocol beyond the two-level manifold and bring the system into even more exotic states by accessing the $\{|g\rangle, |e\rangle, |f\rangle\}$ manifolds. As an example, we aim to thermalize the transmon to a mixture of roughly 50% $|g\rangle$ and 50% $|f\rangle$, as indicated in the bottom right of Fig. 1(d). This is achieved by simultaneously pumping the $|e\rangle \rightarrow |g\rangle$ cooling process at $\omega_{\delta_{s,ge}}$ and the $|e\rangle \rightarrow |f\rangle$ heating process at $\omega_{\Sigma_{s,ef}}$ with matched transition rates away from $|e\rangle$, as shown in Fig. 4(a). The transmon is initialized in the ground state, then both pumps are turned on and the qubit state is readout at the end of the pumps, as shown in Fig. 4(b). The transmon population as a function of time is shown in Fig. 4(c). We note that there is a residual of 15% $|e\rangle$ state which is due to the qubit decay from the $|f\rangle$ state and thermal excitation from the $|g\rangle$ state, as well as the finite measurement fidelity. The simple semi-classical model cannot fully capture the dynamics of this process; we attribute this to the large frequency detuning of the two pump tones in the rotating frame and finite transmon

thermalization rate. By including these factors, we are able to numerically simulate the system's behavior using QuTiP (Appendix E). By going beyond the simple two-level case, we are effectively accessing a certain type of intermediate statistics – Gentile statistics [23–25], where the maximum occupation number of particles in one state is neither infinity (as for Boson) nor one (as for Fermion), but a finite integer n (in our case, $n \geq 2$).

In conclusion, we have experimentally created a controllable multi-level photonic bath for a transmon qubit via parametric interactions between the transmon mode and another cold, lossy bath mode. In the two-level setting, this is equivalent to a tunable chemical potential for the transmon that allows for thermodynamical adjustments, a useful control knob that is typically missing for photons. This will allow us to explore new physics by integrating these controllable bath qubits into larger quantum simulators based on combinations of qubits and cavities arrays, which would benefit from some of its sites having a non-trivial population distribution [22, 38]. On the other hand, this scheme also forms a traditional lambda structure with a trapped excited state, which enables the generation of highly coherent microwave signals [35]. Further, we extended our protocol to the higher levels of the transmon, creating exotic equilibrium states that cannot be realized with a natural thermal bath. This brings interesting perspectives on the experimental study of Gentile statistics, offering opportunities for simulating certain condensed matter systems, such as magnons and spin waves [39].

We acknowledge contributions to earlier versions of this experiment from Guanyu Zhu, Mohammad Hafezi, Mattias Fitzpatrick, Neereja Sundaresan, Basil Smithham, Christie Chou, and Andrew Houck. The TWPA used for amplified readout in this experiment was provided by MIT Lincoln Laboratory. This work was supported by the Army Research Office under Grants No. W911NF15-1-0397 and M. Hatridge's NSF CAREER grant (PHY-1847025). The views and conclusions contained in this document are those of the authors and should be interpreted as representing official policies, either expressed or implied, of the Army Research Office or the US Government. The US Government is authorized to reproduce and distribute reprints for government purposes notwithstanding any copyright notation herein.

Appendix A: Circuit parameters and experiment setup

The qubit frequency is $\omega_q/2\pi = 4.520$ GHz, anharmonicity $\alpha/2\pi = -197.39$ MHz, and its natural decay and heating rates given in the main text are measured by initializing it in different states (Fig. 5). The SAIL-mon frequency (with no external flux applied) is $\omega_{s_0}/2\pi = 9.136$ GHz and its linewidth $\kappa_s/2\pi = 12.98$ MHz. To minimize the undesired higher order effects of the SAIL-mon, we operate at its fourth-order Kerr cancellation point [40], at which the SAIL-mon frequency is $\omega_{s_{\text{op}}}/2\pi = 8.01$ GHz. The hybridization strength $(\frac{g}{\Delta})_{sq} = 1 \times 10^{-2}$, while $(\frac{g}{\Delta})_{sc} = 7 \times 10^{-4}$. The readout cavity has bandwidth $\kappa_c/2\pi = 0.761$ MHz and is followed by a Traveling Wave Parametric Amplifier (TWPA) [34] provided by MIT Lincoln Laboratory through IARPA (see Fig. 6), which allows for single shot readout and clear state differentiation.

The entire experiment was cooled to approximately 20mK on the base stage of a dilution refrigerator, see Fig. 6. Each input drive line is attenuated and filtered with lossy filters made of Eccosorb CR-110 for high frequency light. The external flux threaded through the SAIL-mon's superconducting Josephson junction loop is generated by DC signals of a current source (YOKOGAWA GS200) through superconducting wires. Qubit, pump, and readout pulses are generated by mixing a local oscillator tone with finite single sideband frequency (generated by a SignalCore SC5511A rf signal generator) with the pulses made by an arbitrary waveform generator (Tektronix AWG5014C) with a sampling rate of 1.0 GSa/s using an IQ-mixer (Marki IQ0618).

We measure the reflected signal phase shift from the readout cavity to dispersively infer the qubit's state [29]. The reflected signal is amplified at the base stage by a TWPA, then moves through an Eccosorb filter to prevent high frequency stray photons. It next passes through microwave isolators on the output lines and is amplified using a Low Noise Factory HEMT amplifier at the 4K stage. Once outside of the fridge, the signal is mixed down to 50 MHz using an IR mixer (Marki IR4509) and a local oscillator signal from the SignalCore. The signal is then recorded using a fast ADC card (AlazarTech).

The sample housing, shown in Fig. 7, is comprised of two parts. On one side (left in photo) is a 6061 aluminum coaxial, $\lambda/4$ cavity [41] that acts as our readout resonator. An opening on the side of the coaxial cavity connects to an OFHC copper tube [42] that the sapphire spans to allow for flux biasing the SAIL-mon's Josephson junction loop. The qubit and SAIL-mon are fabricated out of aluminum, with Al/AlOx/Al Josephson junctions, on the same chip of sapphire, via nano-scale lithography. The qubit is positioned between the aluminum and copper housing sections to optimize inter-element couplings. Microwave coupling pins were inserted into the housing, one each per element.

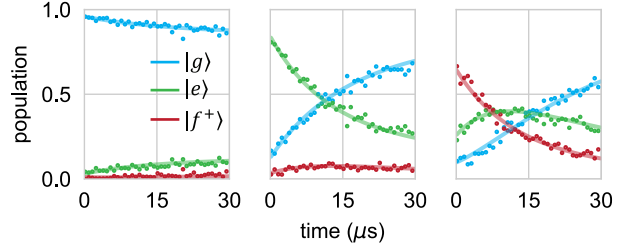


Figure 5. Transmon natural decay measurement. The transmon is prepared in different initial states ($|g\rangle$, $|e\rangle$, and $|f\rangle$ from left to right respectively) and thermalized to its natural steady state with no external pumps applied. The state population is shown as a function of time, and the qubit's natural decay and heating rate can be obtained by fitting it to a semi-classical three-level model.

Appendix B: SAIL-qubit Hamiltonian

The transmon-SAIL-mon Hamiltonian can be written as:

$$H_0/\hbar = \omega_q q^\dagger q + c_4^q (q + q^\dagger)^4 + \omega_s s^\dagger s + c_3^s (s + s^\dagger)^3 + g(s^\dagger q + sq^\dagger), \quad (\text{B1})$$

where ω_q is the transmon frequency, ω_s is the SAIL-mon frequency, g is the capacitive coupling strength between the transmon and SAIL-mon, c_4^q is the coefficient of the transmon's fourth order nonlinearity, and c_3^s is the coefficient of the SAIL-mon's third order nonlinearity. Note here we neglect the fourth order term from the SAIL-mon mode, as it can be largely suppressed at its optimal working point. In addition the Hamiltonian for the SAIL-mon pump is given by:

$$H_{\text{drive}} = \epsilon_d (e^{i(\omega_d t + \phi_d)} s^\dagger + e^{-i(\omega_d t + \phi_d)} s), \quad (\text{B2})$$

where ω_d , ϵ_d , and ϕ_d are the driving frequency, amplitude, and phase respectively.

In the dispersive regime, i.e., $g \ll \Delta = |\omega_s - \omega_q|$, the system can be re-diagonalized under the Bogoliubov transformation [10]. Note that all operators and coefficients are transformed from their original basis, but marked as such for simplicity:

$$H_{\text{sys}}/\hbar = \omega_q q^\dagger q + c_4^q (q + \frac{g}{\Delta} s + \text{h.c.})^4 + \omega_s s^\dagger s + c_3^s (s + \frac{g}{\Delta} q + \text{h.c.})^3 + \epsilon_d (e^{i(\omega_d t + \phi_d)} s^\dagger + e^{-i(\omega_d t + \phi_d)} s) \quad (\text{B3})$$

The drive terms can be removed by moving to a displacement frame with the transformation: $H' = O^\dagger H O - i O^\dagger \dot{O}$, where the transform operator is chosen to be $O_D = \exp(\beta s^\dagger - \beta^* s)$, with $\beta = \epsilon_d e^{-i\phi_d}/(\omega_d - \omega_s)$. The

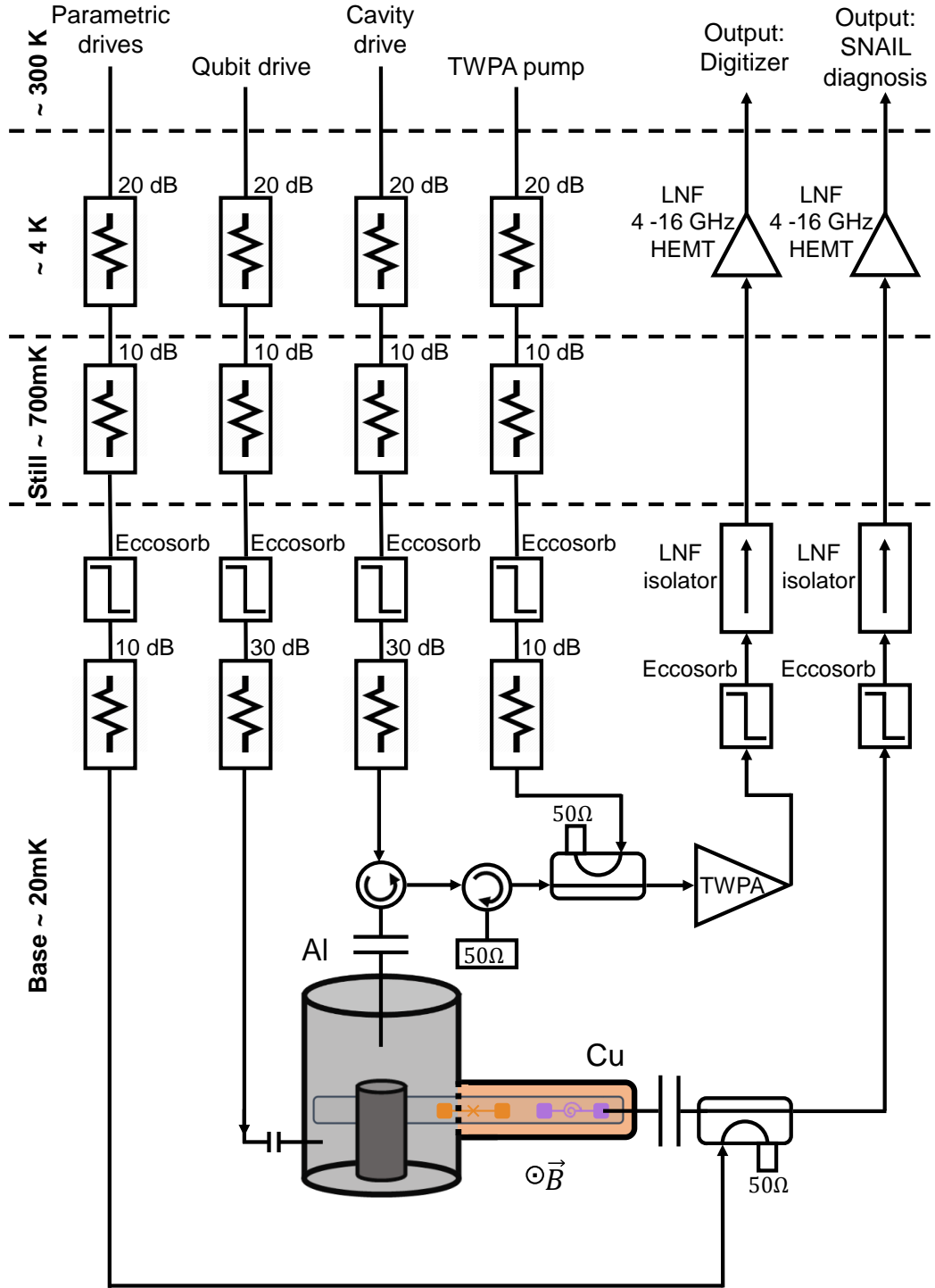


Figure 6. Cryogenic and wiring diagram

system Hamiltonian is then given by:

$$\begin{aligned}
 H_{\text{sys}}/\hbar = & \omega_q q^\dagger q + c_4^q \left(q + \frac{g}{\Delta} (s + \beta e^{i(\omega_d t + \phi_d)}) + \text{h.c.} \right)^4 \\
 & + \omega_s (s + \beta e^{i(\omega_d t + \phi_d)}) (s^\dagger + \beta^* e^{-i(\omega_d t + \phi_d)}) \\
 & + c_3^s \left(s + \beta e^{i(\omega_d t + \phi_d)} + \frac{g}{\Delta} q + \text{h.c.} \right)^3
 \end{aligned} \quad (\text{B4})$$

This can be further simplified by moving into a rotating frame in a similar fashion by choosing the transform

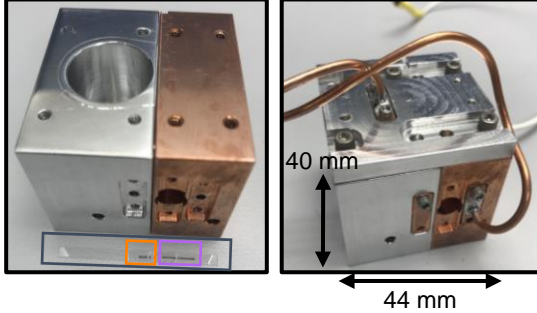


Figure 7. Optical image of the device. We use a two-part package in our experiment. The Al piece is a High-Q coaxial microwave cavity that is used for measuring the qubit. The Cu piece provides a tunnel chip holder that allows flux tuning of the SNAIL-mon. Both the transmon and SNAIL-mon are fabricated on the same sapphire chip and is inserted into the Al cavity through the copper tunnel.

operator to be $O_R = e^{i\omega_s s^\dagger st + i\omega_q q^\dagger qt}$. We get:

$$H_{\text{sys}}/\hbar = 24c_4^q |\beta|^2 q^\dagger q - \alpha q^\dagger qq^\dagger q + c_s^3 (se^{-i\omega_s t} + \frac{g}{\Delta} q e^{-i\omega_q t} + \beta e^{-i\omega_d t} + \text{h.c.})^3. \quad (\text{B5})$$

Here the first term is the qubit Stark shift due the pump, and $\alpha = -6c_4^q$ is the qubit anharmonicity. The effects of the frequency-selected parametric pumps are shown in the third term. Expanding this term B5 produces all possible combinations of SNAIL-mon and qubit operators; most of them can be ignored due to their fast rotations. The pump frequency provides a degree of freedom for selecting the desired processes by matching the frequency of it. In particular, when the SNAIL-mon is driven at $\omega_d = \omega_s + \omega_q$, the qubit-SNAIL-mon Hamiltonian takes the form

$$H_\Sigma/\hbar = 24c_4^q |\beta_\Sigma|^2 q^\dagger q - \alpha q^\dagger qq^\dagger q + g_\Sigma (\beta_\Sigma s^\dagger q^\dagger + \beta_\Sigma^* sq), \quad (\text{B6})$$

where $g_\Sigma = 6c_3^s \frac{g}{\Delta}$. Likewise for the difference frequency pump $\omega_d = \omega_s - \omega_q$:

$$H_\delta/\hbar = 24c_4^q |\beta_\delta|^2 q^\dagger q - \alpha q^\dagger qq^\dagger q + g_\delta (\beta_\delta s^\dagger q^\dagger + \beta_\delta^* sq), \quad (\text{B7})$$

where $g_\delta = 6c_3^s \frac{g}{\Delta}$. Both of these expressions feature pump-induced Stark shifting, the transmon's anharmonicity, and the respective effective 2-body parametric process. Specifically for this application, we restrict the system to only neighboring transitions, allowing us to write Eqs. 3 and 4.

Appendix C: Tunable chemical potential of a parametrically driven qubit

We next derive the steady state population distribution of the qubit in the system shown in Fig. 1(a) and

the expression of its chemical potential. We start with a quick review on a simple model: a qubit coupled to a thermal bath at temperature T_{Bath} . The master equation of the system is given by [43]:

$$\dot{\rho} = \frac{i}{\hbar} [\rho, H] + \frac{\gamma}{2} (\bar{N}(\Omega) + 1) (2\sigma^- \rho \sigma^+ - \rho \sigma^+ \sigma^- + \sigma^+ \sigma^- \rho) + \frac{\gamma}{2} \bar{N}(\Omega) (2\sigma^+ \rho \sigma^- - \rho \sigma^- \sigma^+ + \sigma^- \sigma^+ \rho), \quad (\text{C1})$$

where $H = \frac{\hbar\Omega}{2} \sigma^z$ is the single qubit Hamiltonian, γ is the bandwidth of the qubit mode, Ω is the qubit frequency, $\bar{N}(\Omega) = 1/(e^{\hbar\Omega/kT_{\text{Bath}}} - 1)$ is the average photon number for the thermal state at temperature T_{Bath} . The density matrix at equilibrium is then given by solving the above equation with $\dot{\rho} = 0$:

$$\rho(\infty) = \begin{pmatrix} \frac{1+\bar{N}(\Omega)}{1+2\bar{N}(\Omega)} & 0 \\ 0 & \frac{\bar{N}(\Omega)}{1+2\bar{N}(\Omega)} \end{pmatrix}. \quad (\text{C2})$$

By plugging in the expression of $\bar{N}(\Omega)$, we get:

$$\rho(\infty) = Z(\beta)^{-1} e^{-\beta H}, \quad (\text{C3})$$

where $\beta = 1/k_B T_{\text{Bath}}$, and $Z(\beta) = \text{Tr}(e^{-\beta H})$. The steady state of the qubit is a thermal state at the bath temperature as we expected. Note that in this simple example, the equilibrium state is described by a canonical density operator without a chemical potential.

In our experiment, the setting is more complicated: the qubit is parametrically coupled to the SNAIL-mon, which is also in contact with a thermal bath at temperature T_{Bath} . The Hamiltonian of the system is given by:

$$H_{\text{sys}}/\hbar = \frac{\omega_q}{2} \sigma_q^z + \frac{\omega_s}{2} \sigma_s^z + (g_\Sigma e^{i\omega_\Sigma t} \sigma_s^+ \sigma_q^+ + g_\delta e^{-i\omega_\delta t} \sigma_s^+ \sigma_q^- + \text{h.c.}), \quad (\text{C4})$$

where the SNAIL-mon is also treated as a two-level system under the assumption that its population does not exceed 1 during the qubit thermalization process. This assumption is valid when the bath is cold ($T_{\text{Bath}} \sim 0$) and SNAIL-mon thermalization is much faster than the parametric processes ($\gamma_s \gg g_\Sigma, g_\delta$). With pump frequencies $\omega_\Sigma = \omega_s + \omega_q$ and $\omega_\delta = \omega_s - \omega_q$, we get the Hamiltonian in the rotating frame:

$$H_{\text{sys}}^R/\hbar = g_\Sigma \sigma_s^+ \sigma_q^+ + g_\delta \sigma_s^+ \sigma_q^- + \text{h.c.} \quad (\text{C5})$$

The master equation of this coupled system is given by:

$$\dot{\rho} = \frac{i}{\hbar} [\rho, H_{\text{sys}}^R] + \frac{\gamma_s}{2} (\bar{N}(\omega_s) + 1) (2\sigma^- \rho \sigma^+ - \rho \sigma^+ \sigma^- + \sigma^+ \sigma^- \rho) + \frac{\gamma_s}{2} \bar{N}(\omega_s) (2\sigma^+ \rho \sigma^- - \rho \sigma^- \sigma^+ + \sigma^- \sigma^+ \rho). \quad (\text{C6})$$

For simplicity, we assume that only the SNAIL-mon sees a thermal bath. Similarly, the system density matrix at equilibrium is then given by solving the master equation with $\dot{\rho} = 0$. Let us first look at the SNAIL-mon mode, its density matrix can be obtained by tracing off the qubit degree of freedom $\rho^s = \text{Tr}_q(\rho)$.

$$\begin{aligned}\rho_{00}^s &= \frac{8g_\delta^2 g_\Sigma^2 + (g_\delta^2 + g_\Sigma^2)(1 + \bar{N}(\omega_s))(1 + 2\bar{N}(\omega_s))\gamma_s^2}{16g_\delta^2 g_\Sigma^2 + (g_\delta^2 + g_\Sigma^2)(1 + 2\bar{N}(\omega_s))^2\gamma_s^2} \\ \rho_{01}^s &= 0 \\ \rho_{10}^s &= 0 \\ \rho_{11}^s &= \frac{8g_\delta^2 g_\Sigma^2 + (g_\delta^2 + g_\Sigma^2)\bar{N}(\omega_s)(1 + 2\bar{N}(\omega_s))\gamma_s^2}{16g_\delta^2 g_\Sigma^2 + (g_\delta^2 + g_\Sigma^2)(1 + 2\bar{N}(\omega_s))^2\gamma_s^2}.\end{aligned}\quad (\text{C7})$$

Given that $\gamma_s \gg g_\Sigma, g_\delta$,

$$\frac{g_\delta^2 g_\Sigma^2}{(g_\delta^2 + g_\Sigma^2)\gamma_s^2} \ll 1, \quad (\text{C8})$$

the density matrix simplifies to:

$$\rho^s = \begin{pmatrix} \frac{1+\bar{N}(\omega_s)}{1+2\bar{N}(\omega_s)} & 0 \\ 0 & \frac{\bar{N}(\omega_s)}{1+2\bar{N}(\omega_s)} \end{pmatrix}, \quad (\text{C9})$$

This is a thermal state at the bath temperature, as expected.

The density matrix for the qubit can be obtained in a similar fashion, $\rho^q = \text{Tr}_s(\rho)$:

$$\begin{aligned}\rho_{gg}^q &= \frac{8g_\delta^2 g_\Sigma^2 + (1 + 2\bar{N}(\omega_s))[g_\Sigma^2 \bar{N}(\omega_s) + g_\delta^2(1 + \bar{N}(\omega_s))]\gamma_s^2}{16g_\delta^2 g_\Sigma^2 + (g_\delta^2 + g_\Sigma^2)(1 + 2\bar{N}(\omega_s))^2\gamma_s^2} \\ \rho_{ge}^q &= 0 \\ \rho_{eg}^q &= 0 \\ \rho_{ee}^q &= \frac{g_\delta^2 g_\Sigma^2 + (1 + 2\bar{N}(\omega_s))[g_\delta^2 \bar{N}(\omega_s) + g_\Sigma^2(1 + \bar{N}(\omega_s))]\gamma_s^2}{16g_\delta^2 g_\Sigma^2 + (g_\delta^2 + g_\Sigma^2)(1 + 2\bar{N}(\omega_s))^2\gamma_s^2}.\end{aligned}\quad (\text{C10})$$

We note that the qubit state is a function of the thermal population of the SNAIL-mon mode $\bar{N}(\omega_s)$, this is because we assume that the qubit does not see any other environment other than the SNAIL-mon.

As a sanity check, let us examine the cooling case ($g_\Sigma = 0$), where the qubit has a weak photon exchange interaction with the SNAIL-mon. The qubit density matrix is then reduced to:

$$\rho^q = \begin{pmatrix} \frac{1+\bar{N}(\omega_s)}{1+2\bar{N}(\omega_s)} & 0 \\ 0 & \frac{\bar{N}(\omega_s)}{1+2\bar{N}(\omega_s)} \end{pmatrix}, \quad (\text{C11})$$

The qubit reaches the same thermal state as the SNAIL-mon. This is reasonable, as the qubit will eventually thermalize with the SNAIL-mon through their energy exchanging interaction.

Similarly for the heating case ($g_\delta = 0$), the qubit density matrix is:

$$\rho^q = \begin{pmatrix} \frac{\bar{N}(\omega_s)}{1+2\bar{N}(\omega_s)} & 0 \\ 0 & \frac{1+\bar{N}(\omega_s)}{1+2\bar{N}(\omega_s)} \end{pmatrix}, \quad (\text{C12})$$

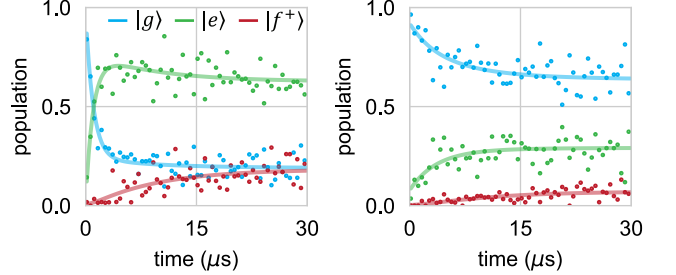


Figure 8. Qubit thermalization with different parametric drive amplitudes. The qubit state population as a function of time is shown for cases where $\Gamma_{ge} > \Gamma_{eg}$ (left) and $\Gamma_{ge} < \Gamma_{eg}$ (right).

where the population inversion is realized as expected [35]. Note here the thermal property of the SNAIL-mon mode ($\bar{N}(\omega_s)$) remains the same, the non-trivial qubit equilibrium is indeed a consequence of parametric bath engineering, rather than simple changing the temperature of the environment.

For a more complicated case, where both pumps are on, we again use the relation in Eq. C8, and get:

$$\rho_{gg}^q = \frac{g_\Sigma^2 \bar{N}(\omega_s) + g_\delta^2(1 + \bar{N}(\omega_s))}{(g_\delta^2 + g_\Sigma^2)(1 + 2\bar{N}(\omega_s))}, \quad (\text{C13})$$

$$\rho_{ee}^q = \frac{g_\delta^2 \bar{N}(\omega_s) + g_\Sigma^2(1 + \bar{N}(\omega_s))}{(g_\delta^2 + g_\Sigma^2)(1 + 2\bar{N}(\omega_s))}. \quad (\text{C14})$$

Again using the expression of $\bar{N}(\omega_s)$, and rearranging to get:

$$P_g^q = \rho_{gg}^q = \frac{1}{1 + e^{-\beta(\hbar\omega_s - \mu)}} \quad (\text{C15})$$

$$P_e^q = \rho_{ee}^q = \frac{e^{-\beta(\hbar\omega_s - \mu)}}{1 + e^{-\beta(\hbar\omega_s - \mu)}}, \quad (\text{C16})$$

where

$$\mu = \frac{1}{\beta} \ln \left(\frac{g_\Sigma^2 e^{\beta \hbar \omega_s} + g_\delta^2}{g_\Sigma^2 e^{-\beta \hbar \omega_s} + g_\delta^2} \right). \quad (\text{C17})$$

Equations C15 and C16 result in a grand canonical density matrix:

$$\rho^q(\infty) = Z(\beta, \mu)^{-1} e^{-\beta(\frac{\omega_s}{2}\sigma_q^z - \frac{\mu}{2}\sigma_q^z)} \quad (\text{C18})$$

where $Z(\beta, \mu) = \text{Tr}[e^{-\beta(\frac{\omega_s}{2}\sigma_q^z - \frac{\mu}{2}\sigma_q^z)}]$, and μ given in Eq. C17 can be identified as the chemical potential of the qubit. The emergence of this chemical potential is a result of two parametric couplings between the qubit and the SNAIL-mon. We can thus tune the chemical potential of the qubit *in situ*, and by extension its equilibrium state, by adjusting the ratio between the two processes' parametric rates, as shown in Fig. 8, as well as Fig. 3 in the main text.

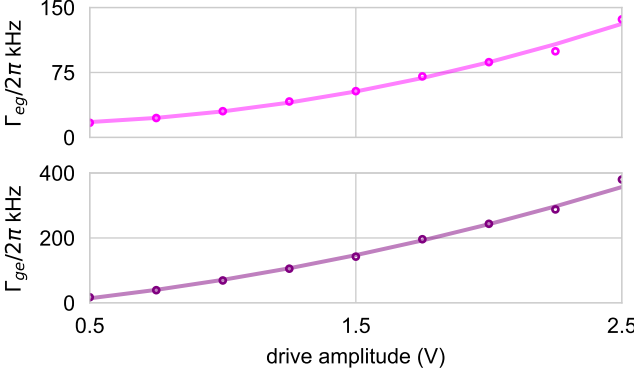


Figure 9. Effective “heating” and “cooling” rate. We show the effective rates of the parametric processes in the cooling (top) and heating (bottom) experiment as a function of room temperature drive voltage. The data fits nicely to a $\gamma_{\Sigma,\delta}$ quadratic model as expected.

Appendix D: Dynamics of qubit thermalization

In the previous section, we discussed the equilibrium state of the qubit when parametrically coupled to a lossy mode. However, the result in Appendix C does not give a description of the dynamics of the process. In order to extract the rates for the heating and cooling processes from the data, we need to have a model to match our experimental results. We start with a simple semi-classical phenomenological model for the two level system. Let P_g and P_e be the probability of the qubit being in the $|g\rangle$ and $|e\rangle$ state, respectively, and the rate jumping from $|g\rangle$ to $|e\rangle$ is Γ_{ge} , from $|e\rangle$ to $|g\rangle$ is Γ_{eg} . The equations for the probabilities are given by:

$$\dot{P}_g = -\Gamma_{ge}P_g + \Gamma_{eg}P_e, \quad (\text{D1})$$

with the condition $P_g + P_e = 1$. The solution to this equation group is:

$$P_g = c_0 e^{-(\Gamma_{ge} + \Gamma_{eg})t} + \frac{\Gamma_{eg}}{\Gamma_{ge} + \Gamma_{eg}}, \quad (\text{D2})$$

where c_0 is a constant to be determined by initial conditions. This model demonstrates the exponential features seen in the heating and cooling data and can be used to extract the relevant rates.

However, to have a full quantum understanding of the process, we need to consider the master equation of the qubit-SNAIL-mon system. In order to obtain an analytical solution, we assume both the SNAIL-mon and qubit can each be described as two-level systems. The assumption is valid for the qubit because of the transmon’s non-zero anharmonicity and for the SNAIL-mon because the large decay rate κ_s reduces the likelihood of higher energy level occupation. We also assume that the two modes are at a physical temperature low enough that their natural heating rates can be ignored. The system Hamiltonian can be written with Pauli matrices (under the rotating

wave approximation):

$$H = g_\Sigma(\sigma_s^+ \sigma_q^+ + \sigma_s^- \sigma_q^-) + g_\delta(\sigma_s^- \sigma_q^+ + \sigma_s^+ \sigma_q^-). \quad (\text{D3})$$

Again, these two terms are the effective two-body terms for the heating and cooling processes respectively. The dynamics of the system’s density matrix ρ are given by the Lindblad master equation:

$$\dot{\rho} = -i[H, \rho] + \kappa_s D(\sigma_s^-)\rho + \kappa_q D(\sigma_q^-)\rho \quad (\text{D4})$$

where $D(a)\rho = a\rho a^\dagger - \frac{1}{2}\{a^\dagger a, \rho\}$ is the term that models the interaction between a mode and its environment, and κ_i is the coupling rate of the i^{th} decay channel.

As an example, let us consider the single heating process. We keep only the SNAIL-mon mode decay term (since $\kappa_s \gg \kappa_q$). Now we may solve a simpler Lindblad master equation:

$$\dot{\rho} = -i[H, \rho] + \kappa_s D(\sigma_s^-)\rho \quad (\text{D5})$$

with $H = g_\Sigma(\sigma_s^+ \sigma_q^+ + \sigma_s^- \sigma_q^-)$. We are interested in the dynamics of the qubit mode $\rho_q = \text{Tr}_s(\rho)$. An analytical solution for the qubit population is available in this case, (for initial state $\rho(0) = |0, g\rangle \langle 0, g|$):

$$P_g = c_1 e^{-\frac{\kappa_s}{2}t} + c_2 e^{-\frac{\kappa_s + \sqrt{(-16g_\Sigma^2 + \kappa_s^2)}}{2}t} + c_3 e^{-\frac{\kappa_s - \sqrt{(-16g_\Sigma^2 + \kappa_s^2)}}{2}t}, \quad (\text{D6})$$

where the coefficients are:

$$c_1 = \frac{8g_\Sigma^2}{16g^2 - \kappa_s^2} \quad (\text{D7})$$

$$c_2 = \frac{8g_\Sigma^2 + \kappa_s(-\kappa_s + \sqrt{-16g_\Sigma^2 + \kappa_s^2})}{32g^2 - 2\kappa_s^2} \quad (\text{D8})$$

$$c_3 = \frac{8g_\Sigma^2 - \kappa_s(-\kappa_s + \sqrt{-16g_\Sigma^2 + \kappa_s^2})}{32g^2 - 2\kappa_s^2} \quad (\text{D9})$$

In the limit $g_\Sigma/\kappa_s \ll 1$, this solution can be further reduced to a simpler form:

$$P_g = e^{-\frac{4g_\Sigma^2}{\kappa_s}t}. \quad (\text{D10})$$

This agrees with Eq. D2 found in the semi-classical case when $\Gamma_{eg} = 0$ and $P_g(0) = 1$ (since we ignore the qubit decay and start in the ground state). We also note that these solutions give results that are consistent with Eqs. C13 and C14 at $t = \infty$ for $\bar{N}(\omega_s) = 0$ (since we treat the bath to be cold). We verify this by sweeping the drive voltages in both the heating and cooling experiment and extract the corresponding rate. In Fig. 9, we show the heating and cooling rate as a function of drive voltages. Both data fit nicely to a quadratic model, thus validating the use of the semi-classical model for rate extraction. We also note that, for the cases where we also

see a non-trivial $|f^+\rangle$ populations, a slightly more complicated semi-classical model that involves the qubit's third level is used for obtaining the rate:

$$\dot{P}_g = -\Gamma_{ge}P_g + \Gamma_{eg}P_e, \quad (\text{D11})$$

$$\dot{P}_e = \Gamma_{ge}P_g - (\Gamma_{ef} + \Gamma_{eg})P_e + \Gamma_{fe}P_f, \quad (\text{D12})$$

with $P_g + P_e + P_f = 1$.

Appendix E: Numerical fitting of a three-level system

The semi-classical model agrees with the data when the pumps only involves the $|g\rangle \leftrightarrow |e\rangle$ manifold. However, the dynamics of the processes that involve pumps connected to all three levels cannot be nicely captured by it, as shown in Fig. 10. Here we go beyond the theoretical model and numerically study our system to understand its behavior in the three-level manifold. The effective Hamiltonian under the rotating wave approximation (in the frame rotating at ω_{ge}) is:

$$H = -\alpha q^\dagger q q^\dagger q + (g_{\Sigma_{s,ef}} e^{i\alpha t} s^\dagger q^\dagger + \text{h.c.}) + (g_{\delta_{s,ge}} s^\dagger q + \text{h.c.}) \quad (\text{E1})$$

We note that in the ω_{ge} frame, there will always be time dependent terms that rotate at anharmonicity frequency α for the $|kete \leftrightarrow |f\rangle$ manifold drives. The full Lindblad master equation is given by:

$$\dot{\rho} = -i[H, \rho] + \kappa_s D(s)\rho + \kappa_q^\downarrow D(q)\rho + \kappa_q^\uparrow D(q^\dagger)\rho. \quad (\text{E2})$$

Here in the dissipator terms, we consider both the decay of the SQUID-mon and qubit (with collapse operator s and q at rate κ_s and κ_q^\downarrow) and also the natural heating of the qubit due to the finite temperature (with collapse operator q^\dagger at rate κ_q^\uparrow). This equation is then simulated using QuTiP. We also take into account the up-pumped qubit thermalization during the measurement process, this is modeled by turning off the pump tone in the Hamiltonian and letting the system evolve for the time of measurement.

The parameters used for the simulation we show in Fig. 4(b) are as follows: $\alpha/2\pi = 197$ MHz, $\kappa_s/2\pi = 12.98$ MHz, $\kappa_q^\downarrow/2\pi = 0.029$ MHz, $\kappa_q^\uparrow/2\pi = 0.006$ MHz and measurement time $\tau_{msmt} = 1.2$ μ s. We note that the qubit decay rate used in the simulation is equivalent to a qubit with $T_1 \sim 4.5$ μ s, which is faster than the transmon's natural decoherence rate. We attribute this to the faster decay rate of higher transmon levels and possible qubit coherence time reduction due to large pump photon numbers, which could invalidate the assumptions we used for the semi-classical model.

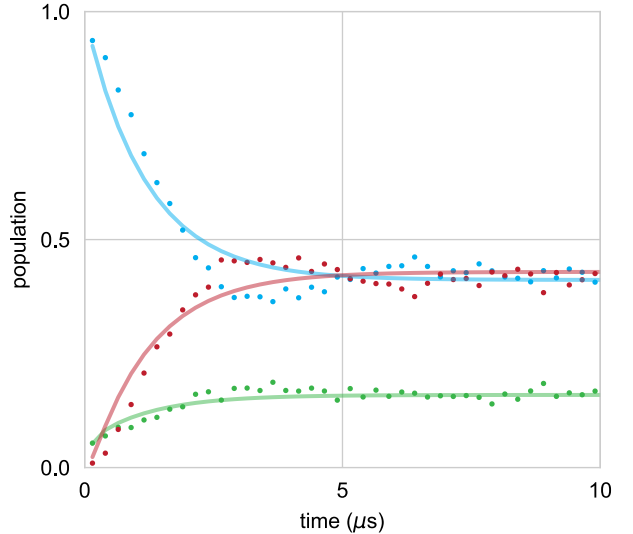


Figure 10. Three-level multi-pump data fit with semi-classical mode. The population of different energy level as a function of time. Here we zoom in on the first 10 μ s of the data shown in Fig. 4(b). The data is fit to the semi-classical model introduced in Appendix D. While the model can predict the steady state population, it does not fully capture the dynamics of the entire process.

-
- [1] R. P. Feynman, International Journal of Theoretical Physics **21**, 467 (1982).
- [2] M. Lewenstein, A. Sanpera, V. Ahufinger, B. Damski, A. Sen, and U. Sen, Advances in Physics **56**, 243 (2007).
- [3] M. J. Gingras and P. A. McClarty, Reports on Progress in Physics **77**, 056501 (2014).
- [4] M. Reiher, N. Wiebe, K. M. Svore, D. Wecker, and M. Troyer, Proceedings of the National Academy of Sciences **114**, 7555 (2017).
- [5] S. Krinner, T. Esslinger, and J.-P. Brantut, Journal of Physics: Condensed Matter **29**, 343003 (2017).
- [6] F. Giazotto, T. T. Heikkilä, A. Luukanen, A. M. Savin, and J. P. Pekola, Reviews of Modern Physics **78**, 217 (2006).
- [7] D. A. Abanin, E. Altman, I. Bloch, and M. Serbyn, Reviews of Modern Physics **91**, 021001 (2019).
- [8] F. Harper, R. Roy, M. S. Rudner, and S. Sondhi, Annual Review of Condensed Matter Physics **11**, 345 (2020).
- [9] B. Swingle, Nature Physics **14**, 988 (2018).
- [10] A. Blais, A. L. Grimsrud, S. M. Girvin, and A. Wallraff, Reviews of Modern Physics **93**, 025005 (2021).
- [11] C. Monroe, W. C. Campbell, L.-M. Duan, Z.-X. Gong, A. V. Gorshkov, P. W. Hess, R. Islam, K. Kim, N. M. Linke, G. Pagano, *et al.*, Reviews of Modern Physics **93**, 025001 (2021).
- [12] S. Slussarenko and G. J. Pryde, Applied Physics Reviews **6**, 041303 (2019).
- [13] A. A. Houck, H. E. Türeci, and J. Koch, Nature Physics **8**, 292 (2012).
- [14] I. Carusotto, A. A. Houck, A. J. Kollár, P. Roushan, D. I. Schuster, and J. Simon, Nature Physics **16**, 268 (2020).
- [15] P. M. Harrington, E. J. Mueller, and K. W. Murch, Nature Reviews Physics **4**, 660 (2022).
- [16] M. Planck, *The theory of heat radiation* (Blakiston, 1914).
- [17] C. H. Henry and R. F. Kazulinov, Reviews of Modern Physics **68**, 801 (1996).
- [18] J. Klaers, J. Schmitt, F. Vewinger, and M. Weitz, Nature **468**, 545 (2010).
- [19] J. Klaers, J. Schmitt, T. Damm, F. Vewinger, and M. Weitz, Physical Review Letters **108**, 160403 (2012).
- [20] K. Geerlings, Z. Leghtas, I. M. Pop, S. Shankar, L. Frunzio, R. J. Schoelkopf, M. Mirrahimi, and M. H. Devoret, Physical Review Letters **110**, 120501 (2013).
- [21] Y. Lu, S. Chakram, N. Leung, N. Earnest, R. K. Naik, Z. Huang, P. Groszkowski, E. Kapit, J. Koch, and D. I. Schuster, Physical Review Letters **119** (2017).
- [22] R. Ma, B. Saxberg, C. Owens, N. Leung, Y. Lu, J. Simon, and D. I. Schuster, Nature **566**, 51 (2019).
- [23] G. Gentile j, Il Nuovo Cimento (1924-1942) **17**, 493 (1940).
- [24] W.-S. Dai and M. Xie, Annals of Physics **309**, 295 (2004).
- [25] C. Srivatsan, M. Murthy, and R. Bhaduri, Pramana **66**, 485 (2006).
- [26] M. Hafezi, P. Adhikari, and J. Taylor, Physical Review B **92**, 174305 (2015).
- [27] J. Koch, T. M. Yu, J. Gambetta, A. A. Houck, D. I. Schuster, J. Majer, A. Blais, M. H. Devoret, S. M. Girvin, and R. J. Schoelkopf, Physical Review A **76**, 042319 (2007).
- [28] N. E. Frattini, U. Vool, S. Shankar, A. Narla, K. M. Sliwa, and M. H. Devoret, Applied Physics Letters **110**, 222603 (2017).
- [29] A. Blais, R.-S. Huang, A. Wallraff, S. M. Girvin, and R. J. Schoelkopf, Physical Review A **69**, 062320 (2004).
- [30] A. Roy and M. Devoret, Comptes Rendus Physique **17**, 740 (2016).
- [31] A. Kamal, A. Marblestone, and M. Devoret, Physical Review B **79**, 184301 (2009).
- [32] N. Bergeal, F. Schackert, M. Metcalfe, R. Vijay, V. E. Manucharyan, L. Frunzio, D. E. Prober, R. J. Schoelkopf, S. M. Girvin, and M. H. Devoret, Nature **465**, 64 (2010).
- [33] J. M. Gertler, B. Baker, J. Li, S. Shirol, J. Koch, and C. Wang, Nature **590**, 243 (2021).
- [34] C. Macklin, K. O'Brien, D. Hover, M. E. Schwartz, V. Bolkhovsky, X. Zhang, W. D. Oliver, and I. Siddiqi, Science **350**, 307 (2015).
- [35] C. Liu, M. Mucci, X. Cao, M. V. G. Dutt, M. Hatridge, and D. Pekker, Nature Communications **12** (2021).
- [36] C. Zhou, *Superconducting Quantum Routers, Modules, Gates, and Measurements Based on Charge-pumped Parametric Interactions*, Ph.D. thesis, University of Pittsburgh (2024).
- [37] L. Stefanazzi, K. Treptow, N. Wilcer, C. Stoughton, C. Bradford, S. Uemura, S. Zorzetti, S. Montella, G. Cancelo, S. Sussman, A. Houck, S. Saxena, H. Arnaldi, A. A, H. Zhang, C. Ding, and D. I. Schuster, Rev. Sci. Instrum. **93**, 044709 (2022).
- [38] A. J. Kollar, M. Fitzpatrick, and A. A. Houck, Nature **571**, 45 (2019).
- [39] Y. Shen, C.-C. Zhou, and Y.-Z. Chen, Physica A: Statistical Mechanics and its Applications **596**, 127223 (2022).
- [40] V. V. Sivak, N. E. Frattini, V. R. Joshi, A. Lingenfelter, S. Shankar, and M. H. Devoret, Physical Review Applied **11**, 5 (2019).
- [41] M. Reagor, H. Paik, G. Catelani, L. Sun, C. Axline, E. Holland, I. M. Pop, N. A. Masluk, T. Brecht, L. Frunzio, M. H. Devoret, L. Glazman, and R. J. Schoelkopf, Applied Physics Letters **102**, 192604 (2013).
- [42] C. Axline, M. Reagor, R. Heeres, P. Reinhold, C. Wang, K. Shain, W. Pfaff, Y. Chu, L. Frunzio, and R. J. Schoelkopf, Applied Physics Letters **109**, 042601 (2016).
- [43] C. Gardiner and P. Zoller, *Quantum noise: a handbook of Markovian and non-Markovian quantum stochastic methods with applications to quantum optics* (Springer Science & Business Media, 2004).